Tomographic SAR Inversion by L_1-Norm Regularization—The Compressive Sensing Approach

Xiao Xiang Zhu, *Student Member, IEEE*, and Richard Bamler, *Fellow, IEEE*

***Abstract*—Synthetic aperture radar (SAR) tomography (TomoSAR) extends the synthetic aperture principle into the elevation direction for 3-D imaging. The resolution in the elevation direction depends on the size of the elevation aperture, i.e., on the spread of orbit tracks. Since the orbits of modern meter-resolution spaceborne SAR systems, like TerraSAR-X, are tightly controlled, the tomographic elevation resolution is at least an order of magnitude lower than in range and azimuth. Hence, super-resolution reconstruction algorithms are desired. The high anisotropy of the 3-D tomographic resolution element renders the signals *sparse* in the elevation direction; only a few pointlike reflections are expected per azimuth–range cell. This property suggests using compressive sensing (CS) methods for tomographic reconstruction. This paper presents the theory of 4-D (differential, i.e., space–time) CS TomoSAR and compares it with parametric (nonlinear least squares) and nonparametric (singular value decomposition) reconstruction methods. Super-resolution properties and point localization accuracies are demonstrated using simulations and real data. A CS reconstruction of a building complex from TerraSAR-X spotlight data is presented.**

***Index Terms*—Compressive sensing (CS), differential synthetic aperture radar tomography (D-TomoSAR), TerraSAR-X, urban mapping.**

I. Introduction

SYNTHETIC aperture radar (SAR), SAR tomography (TomoSAR) [1] extends the synthetic aperture principle of SAR into the elevation direction for 3-D imaging. It uses acquisitions from slightly different viewing angles (the elevation aperture) to reconstruct for every azimuth–range $(x-r)$ pixel the reflectivity function along the elevation direction s, i.e., the third dimension perpendicular to x and r (Fig. 1). It is essentially a spectral analysis problem. *Differential* SAR tomography (TomoSAR) [2], also referred to as 4-D focusing, obtains a 4-D (space–time) map of scatterers by estimating both the elevation and the deformation velocity of multiple scatterers inside an azimuth–range resolution cell.

Manuscript received October 6, 2009; revised January 20, 2010. Date of publication June 7, 2010; date of current version September 24, 2010.

X. Zhu is with the Technische Universität München, Lehrstuhl für Methodik der Fernerkundung, 80333 Munich, Germany (e-mail: xiaoxiang.zhu@bv.tum.de).

R. Bamler is with the Remote Sensing Technology Institute (IMF), German Aerospace Center (DLR), 82234 Oberpfaffenhofen, Germany, and also with the Technische Universität München, Lehrstuhl für Methodik der Fernerkundung, 80333 Munich, Germany (e-mail: richard.bamler@dlr.de).

Color versions of one or more of the figures in this paper are available online at http://ieeexplore.ieee.org.

Digital Object Identifier 10.1109/TGRS.2010.2048117

The first experiments in TomoSAR were carried out in the laboratory [3] under ideal experimental conditions or by using airborne systems [1]. Spaceborne TomoSAR tests were reported in [4] and [5]. It has been applied to C-band ERS data over extended scenes in [6] and to TerraSAR-X data in [7]. In [8], the single- and double-scatterer cases were separated. The concept of 4-D SAR imaging (differential TomoSAR) was proposed in [2] and first applied to ERS data in [9].

With the German TerraSAR-X and the Italian COSMO-Skymed satellites, SAR data with a very high spatial resolution (VHR) of up to 1 m are available. This resolution is particularly helpful when it comes to interferometric and tomographic imaging of buildings and urban infrastructure. The inherent spatial scales of these objects are in the meter range (e.g., typical height between floors of 3–3.5 m).

We work with TerraSAR-X high-resolution *spotlight* data. These VHR X-band spaceborne repeat-pass tomographic data stacks of urban areas have some particular properties. A very detailed view of individual buildings is possible. The density of bright points, like persistent scatterers, is extremely high (up to 100 000/km^2). However, nonlinear (e.g., thermal-induced) deformations of different building parts must also be expected and will introduce additional phase errors, if not modeled. Due to the tight orbit tube of TerraSAR-X, the elevation aperture is small, i.e., the inherent resolution in elevation is about 50 times worse than that in azimuth or range. This extreme anisotropy calls for super-resolution algorithms in the elevation direction. Finally, VHR data are expensive, and hence, data stacks should be kept small. There are several super-resolving methods, such as CAPON, MUSIC, etc. They are discussed in detail in [10]–[12]. We concentrate on methods that do not require averaging in azimuth and range in order to fully exploit the potential of this class of VHR data.

Compressive sensing (CS) [13]–[16], as a favorable sparse reconstruction technique, is a new and attractive method for TomoSAR. It aims at minimizing the number of measurements to be taken from signals while still retaining the information necessary to approximate them well. It provides a good compromise between classical parametric and nonparametric spectral analysis methods. Compared to parametric spectral analysis, CS is more robust to phase noise, has lower computational effort, and does not require model selection to provide the prior knowledge about the number of scatterers in a resolution cell. Compared to nonparametric spectral estimation, CS has no interference problem and it overcomes the limitation of elevation resolution caused by the extent of elevation aperture, i.e., CS has super-resolution properties.

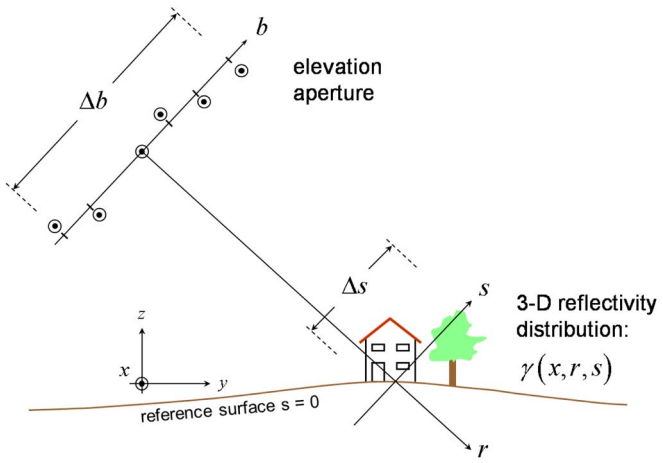

Fig. 1. TomoSAR imaging geometry. The coordinate s is referred to as elevation, and b (parallel to s) is regarded as aperture position.

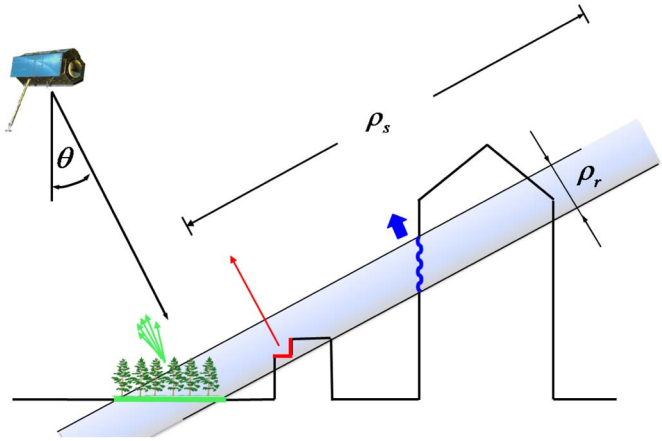

Fig. 2. Possible signal contributions in a single SAR image azimuth–range pixel. ρ_r and ρ_s: range and elevation resolutions, respectively (size of resolution cells not to scale).

Motivated by recent work on inverse SAR [17] and first TomoSAR simulations [18], the CS approach to TomoSAR is outlined in this paper. Its extension to differential (4-D) TomoSAR is introduced. Numerical simulations for realistic acquisition and noise scenarios will be presented to evaluate the potential and limits of the technique. The first CS TomoSAR results with TerraSAR-X spotlight data over urban areas will be presented.

II. Signal and Noise Model

In VHR X-band data, we expect the following signal contributions (see Fig. 2) [19].

1) Weak diffuse scattering from—mostly horizontal or vertical—rough surfaces (roads and building walls). These objects have an elevation extent of $\rho_r/\tan(\theta-\alpha)$, where ρ_r is the (slant)-range resolution, θ is the local incidence angle, and α is the slope of the surface relative to horizontal. Except from large surfaces accidentally oriented along elevation, these responses are of much smaller extent than the elevation resolution ρ_s, and hence, they can be treated as discrete scatterers in the elevation direction (delta functions).
2) Strong returns from metallic structures or specular and dihedral or trihedral reflections. These are points that would also be used in persistent scatterer interferometry. They are the dominating signal contributions. With VHR SAR data, the density of these points can be very high.
3) Returns from volumetric scatterers, e.g., from vegetation. These result in a continuous-signal background in elevation. These ensembles of scatterers, however, often decorrelate in time, and their response is therefore treated as noise.

The noise sources are the following.

1) Gaussian noise, which is caused by thermal noise and temporal decorrelation, as mentioned earlier.
2) Calibration errors in amplitude. The radiometric stability of TerraSAR-X, i.e., the amplitude variations within one stack, is 0.14 dB and is therefore negligible compared to our typical signal-to-noise ratio (SNR).
3) Phase errors caused by atmospheric delay and unmodeled motion. They require robust and phase-error-tolerant estimation methods.

These considerations suggest that the elevation signal to be reconstructed is *sparse* in the object domain, i.e., it can be described by a few (typically one to three) pointlike contributions of unknown positions and unknown amplitudes and phases. Sparsity is the central concept of and a prerequisite for CS.

III. TomoSAR Imaging Model

For a single SAR acquisition, the focused complex-valued measurement $g_n(x_0,r_0)$ of an azimuth–range pixel (x_0,r_0) for the nth acquisition at aperture position b_n and at time t_n is the integral (tomographic projection) of the reflected signal along the elevation direction [20], as shown in Fig. 1 (the deformation term is ignored here for simplicity) [9]

$$g_n = \int_{\Delta s} \gamma(s)\exp(-j2\pi\xi_n s)\,ds, \qquad n=1,\ldots,N \tag{1}$$

where $\gamma(s)$ represents the reflectivity function along elevation s. $\xi_n=-2b_n/(\lambda r)$ is the spatial (elevation) frequency. The continuous-space system model of (1) can be approximated by discretizing the continuous-reflectivity function along s (ignoring an inconsequential constant)

$$\mathbf{g}=\mathbf{R}\boldsymbol{\gamma} \tag{2}$$

where $\mathbf{g}$ is the measurement vector with N elements g_n, $\mathbf{R}$ is an $N\times L$ mapping matrix with $R_{nl}=\exp(-j2\pi\xi_n s_l)$, and $\boldsymbol{\gamma}$ is the discrete reflectivity vector with L elements $\gamma_l=\gamma(s_l)$. s_l $(l=1,\ldots,L)$ denotes the discrete elevation positions. Equation (1) is an irregularly sampled discrete Fourier transform of the elevation profile $\gamma(s)$. The objective of TomoSAR is to retrieve the reflectivity profile for each azimuth–range pixel.

The extension to the 4-D (space-time) case is straightforward [2], [19]. Taking the motion term into account, the system model (1) can be extended to

$$g_n = \int_{\Delta s} \gamma(s)\exp(-j2\pi\left(\xi_n s+\eta_n V(s)\right))\,ds, \qquad n=1,\ldots,N \tag{3}$$

where $V(s)$ is the deformation line-of-sight (LOS) velocity profile along elevation, and $\eta_n = 2t_n/\lambda$ may, in analogy, be called a "velocity frequency." Formally, (3) can be rewritten as

$$g_n = \int_{\Delta v}\int_{\Delta s} \gamma(s)\delta\left(v - V(s)\right)\exp\left(-j2\pi(\xi_n s + \eta_n v)\right) ds\, dv, \quad n = 1, \ldots, N \tag{4}$$

where Δv is the range of possible velocities. Equation (4) is a 2-D Fourier transform of $\gamma(s)\delta(v - V(s))$, which is a delta line in the elevation–velocity $(s{-}v)$ plane along $v = V(s)$. Its projection onto the elevation axis $\gamma(s)\delta(v - V(s))$ is the reflectivity profile $\gamma(s)$. If we accept $\gamma(s)\delta(v - V(s))$ as the object to be reconstructed, the discretized system model of (2) is easily adopted and simply becomes a 2-D Fourier transform [2], [9]. Its inversion provides retrieval of the elevation and deformation information even of multiple scatterers inside an azimuth–range resolution cell and thus obtains a 4-D map of scatterers. It is required for reliable 3- and 4-D city mapping from repeat-pass acquisitions.

IV. TomoSAR via CS

A. CS

CS is a new and popular approach for sparse signal reconstruction. A signal of interest $\mathbf{x}$ with a length of L is said to be K-sparse in an orthogonal basis $\mathbf{\Psi}$ if the projection coefficient vector $\mathbf{s} = \mathbf{\Psi x}$ has only K nonzero or significant elements. $\mathbf{x}$ is represented by $\mathbf{\Psi^H s}$. N measurements $\mathbf{y}$ can be obtained by projecting the signal onto N random basis functions $\mathbf{\Phi}$ (the sensing matrix)

$$\mathbf{y} = \mathbf{\Phi x}. \tag{5}$$

The measurement vector can be rewritten as

$$\mathbf{y} = \mathbf{\Phi\Psi^H s} = \mathbf{\Theta s}. \tag{6}$$

Within the CS framework, $\mathbf{s}$ can be reconstructed by L_0-norm minimization, i.e., by finding the solution of (6) employing the least number of coefficients

$$\min_{\mathbf{s}} \|\mathbf{s}\|_0 \quad \text{s.t.} \quad \mathbf{y} = \mathbf{\Theta s}. \tag{7}$$

For $N = O(K\log(L/K))$, it can be shown that L_1-norm minimization leads to the same result as L_0-norm minimization [21]

$$\min_{\mathbf{s}} \|\mathbf{s}\|_1 \quad \text{s.t.} \quad \mathbf{y} = \mathbf{\Theta s}. \tag{8}$$

However, the following conditions must hold in order to find the unique sparse solution.

First, the sensing matrix $\mathbf{\Phi}$ and the orthogonal basis $\mathbf{\Psi}$ must be mutually *incoherent*. Incoherence means that the orthogonal projection by $\mathbf{\Psi}$ will spread out information of sparse (highly localized) signals in the entire projection space and thus makes them insensitive to "undersampling." Otherwise, the reconstruction of nonzero coefficients will be biased toward certain positions. For instance, let us randomly choose N columns from $\mathbf{\Psi}$ as our sensing matrix $\mathbf{\Phi}$. Then, what we are actually sensing with $\mathbf{\Theta}$ is only the N elements of $\mathbf{s}$ located at the positions of the N randomly chosen columns. As a consequence of this counterexample, the sparse reconstruction would only be possible if the K nonzero coefficients were located within the N chosen positions.

Second, the mapping matrix $\mathbf{\Theta}$ must follow the *restricted isometry property* (RIP) to guarantee the sufficiently sparse reconstruction in the presence of noise. The RIP requires that

$$(1 - \delta_s)\|\mathbf{v}\|_2^2 \le \|\mathbf{\Theta v}\|_2^2 \le (1 + \delta_s)\|\mathbf{v}\|_2^2 \tag{9}$$

where $\mathbf{v}$ is any vector having K nonzero coefficiencs at the same positions as $\mathbf{s}$ and δ_s is a small number. The smaller the δ_s is, the better the sparse signal can be reconstructed in the presence of noise. Equation (9) essentially says that all submatrices of $\mathbf{\Theta}$ composed of K significant columns should be nearly orthogonal and hence preserve the length of the vectors sharing the same K nonzero coefficients as $\mathbf{s}$. There are some well-known pairs of incoherent bases, such as randomly selected Fourier samples as the sensing matrix and the identity matrix as the orthogonal basis, as well as the Gaussian sensing matrix and any other basis.

Therefore, in order to understand whether CS is applicable for a specific problem or not, one should check first the sparsity of signal, the required minimum number of measurements, the incoherence, and the RIP.

B. TomoSAR via CS

As described in Section II, for VHR spaceborne X-band TomoSAR, the elevation signal $\boldsymbol{\gamma}$ to be reconstructed is *sparse* in the object domain with typically one to three pointlike contributions of unknown positions and unknown amplitudes and phases, i.e., $\boldsymbol{\gamma}$ is sparse in the identity orthogonal basis $(\mathbf{\Psi} = \mathbf{I})$. According to (1) and (2), the sensing matrix $\mathbf{\Phi} = \mathbf{R}$ is a randomly distributed Fourier sampling matrix that has the best incoherence property with our identity orthogonal basis $\mathbf{I}$. Due to the small K, $N = O(K\log(L/K))$ can be very easily fulfilled; hence, the K-sparse signal $\boldsymbol{\gamma}$ can be exactly recovered in the absence of noise by L_1 minimization

$$\min_{\boldsymbol{\gamma}} \|\boldsymbol{\gamma}\|_1 \quad \text{s.t.} \quad \mathbf{g} = \mathbf{R}\boldsymbol{\gamma}. \tag{10}$$

In case there is no prior knowledge about K and in the presence of measurement noise, it can be approximated by

$$\hat{\boldsymbol{\gamma}} = \arg\min_{\boldsymbol{\gamma}} \left\{\|\mathbf{g} - \mathbf{R}\boldsymbol{\gamma}\|_2^2 + \lambda_K\|\boldsymbol{\gamma}\|_1\right\} \tag{11}$$

where λ_K is a factor adjusted according to the noise level. The choice of λ_K is described in great detail in [22]. This equation can be solved by basis pursuit methods [23]. Instead of detecting K most significant coefficients, it tries to minimize the residual by employing an L_1-norm regularization. By providing the overcompleteness of $\boldsymbol{\gamma}$ (i.e., several close spectral lines for one scatterer instead of single spectral line), it can provide more robust solutions.

With the given elevation aperture positions, the RIP properties can be checked.

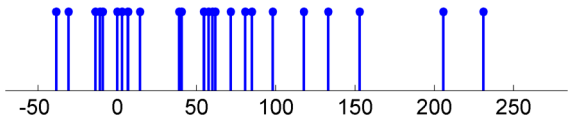

Fig. 3. Elevation aperture positions (in meters).

V. Experiments

A. Data Set

For the purpose of this paper, we work with TerraSAR-X spotlight data with a slant-range resolution of 0.6 m and an azimuth resolution of 1 m [24]. Our test site is Las Vegas, NV, U.S. The acquisition repeat cycle is 11 days. The orbit of TerraSAR-X is controlled in a predefined tube of 500-m diameter throughout the entire mission [25]. A data stack of 25 scenes is used for our experiment. The elevation aperture sampling positions are shown in Fig. 3. The elevation aperture size Δb is about 269.5 m.

For nonparametric linear spectral analysis, the expected elevation resolution ρ_s, i.e., the width of the elevation point response function, depends on the elevation aperture length Δb and is approximately (sufficiently dense and regular sampling of the elevation aperture provided)

$$\rho_s = \frac{\lambda r}{2\Delta b} = 40.5 \text{ m} \tag{12}$$

or about 20 m in height (z) at an incidence angle of 31.8° [19]. This, however, does not mean that individual scatterers can only be located to within this poor elevation resolution. The Cramér–Rao lower bound (CRLB) on elevation estimates can be shown to be asymptotically (high-SNR approximation) [26]

$$\sigma_{\hat{s}} = \frac{\lambda r}{4\pi\sqrt{NOA}\cdot\sqrt{2SNR}\cdot\sigma_b} \tag{13}$$

where NOA is the number of acquisitions, SNR is the signal-to-noise ratio of the individual scatterer, and σ_b is the standard deviation of the elevation aperture sampling distribution. The stack used in this example has $\sigma_b = 70.9$ m. For many bright points, we can assume a SNR of 10 dB; then, the CRLB on elevation estimation is 1.1 m, i.e., almost 1/40 of the elevation resolution.

With our elevation aperture position distribution, the RIP requirement of (9) is perfectly met in the case of a single scatterer. That is trivial. For two scatterers of equal reflectivity and phase, the quantity δ_s of (9) is a function of the scatterers' distance (Fig. 4). It increases once the scatterers come closer than the resolution ρ_s. In other words, the closer the two scatterers are, the more sensitive the reconstruction becomes to noise, which leads to a lower probability of separating close scatterers. Distinguishing closer scatterers robustly requires higher SNR, which will be discussed in more detail later.

B. Simulated Data

In this section, the CS approach is compared to conventional nonparametric and parametric methods using simulated data. The data are simulated using the elevation aperture distribution of Fig. 3 (elevation resolution $\rho_s = 40.5$ m). The decorrelation effect is introduced by adding Gaussian noise

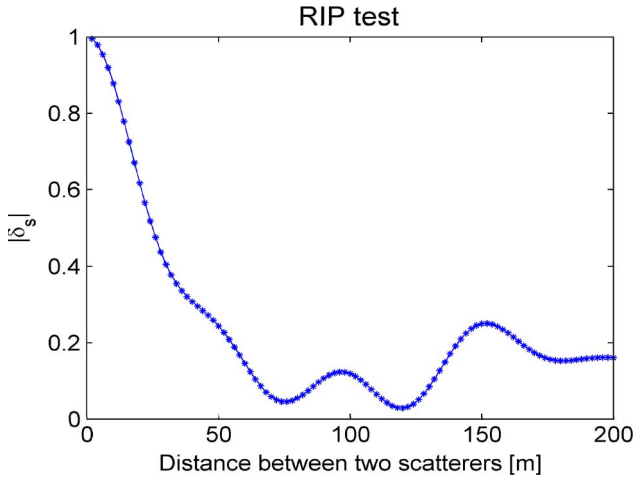

Fig. 4. RIP property of two scatterers with the same reflectivity (i.e., amplitude and phase). δ_s refers to (9).

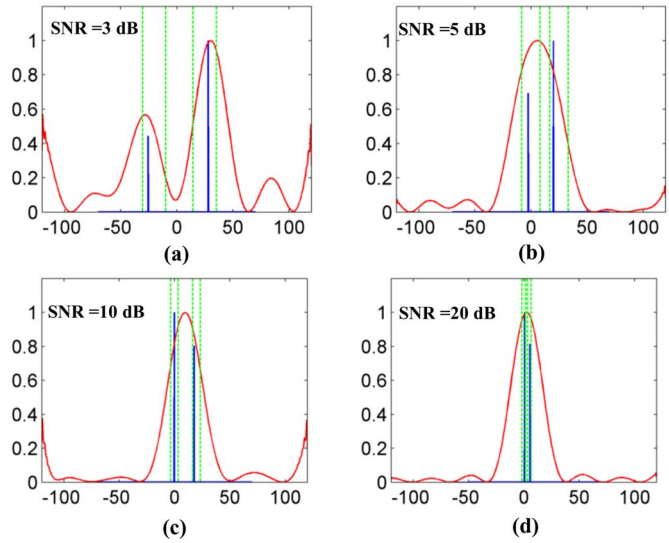

Fig. 5. Comparison of the reconstructed reflectivity profiles along the elevation direction between SVD-Wiener and CS. (Red solid lines) SVD-Wiener. (Blue solid lines) CS. (Green dashed lines) ± 3 times CRLB. (a) Two scatterers with $s_1 = -20$ m and $s_2 = 25$ m (total SNR $= 3$ dB). (b) Two scatterers with $s_1 = 0$ m and $s_2 = 25$ m (SNR $= 5$ dB). (c) Two scatterers with $s_1 = 0$ m and $s_2 = 20$ m (SNR $= 10$ dB). (d) Two scatterers with $s_1 = 0$ m and $s_2 = 5$ m (SNR $= 20$ dB).

with different SNR. Phase noise due to unmodeled deformation and atmospheric effects are simulated by adding a uniformly distributed phase.

Fig. 5 shows the comparison of the reconstructed reflectivity profiles along the elevation direction between a singular value decomposition (SVD) reconstruction with Wiener-type regularization (SVD-Wiener) [19] and CS. The red lines represent the reconstruction using the nonparametric method SVD-Wiener. The blue lines show the same result using CS. We start with two scatterers with elevations of -25 and 20 m [Fig. 5(a)] with total SNR $= 3$ dB (i.e., for each of the two scatterers: SNR $= 0$ dB). CS reconstructs spectral lines instead of sinclike point response functions. Both methods can distinguish the two scatterers well. However, once they move close into one elevation resolution cell with elevations of 0 and 25 m, SVD-Wiener is no longer able to distinguish them. CS detects very

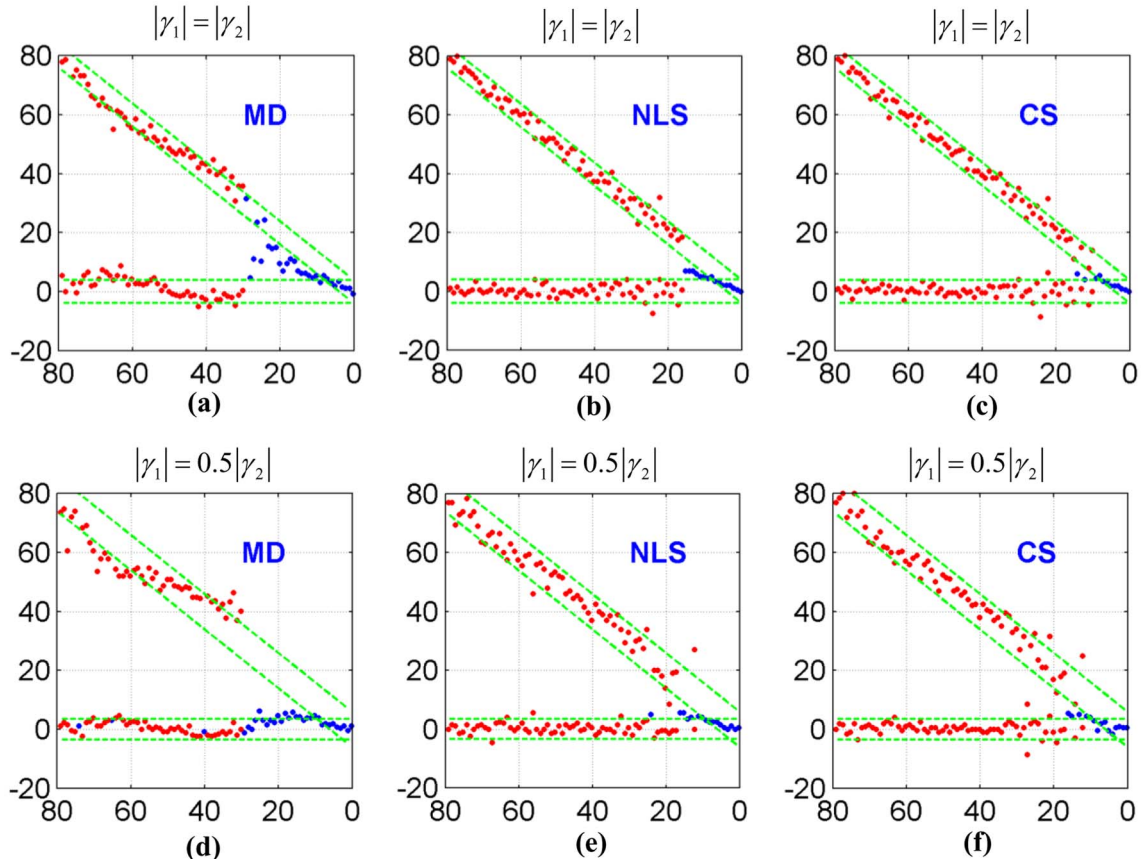

Fig. 6. Estimated elevations (in meters) of two scatterers of equal phase of increasing elevation distance. Shown are the results of (a) and (d) MD, (b) and (e) NLS estimation, and (c) and (f) CS, with total SNR = 10 dB under different reflectivity ratio. (Upper plots) The two scatterers have the same reflectivity. (Lower plots) The reflectivity of the scatterer on the building facade is 0.5 times of the one on the ground. The true positions are a horizontal line referring to the ground and a diagonal line referring to the scatterer at variable elevation. The green dashed lines show ± 3 times the CRLB of elevation estimates for single scatterers (blue: detected single scatterer; red: detected two scatterers).

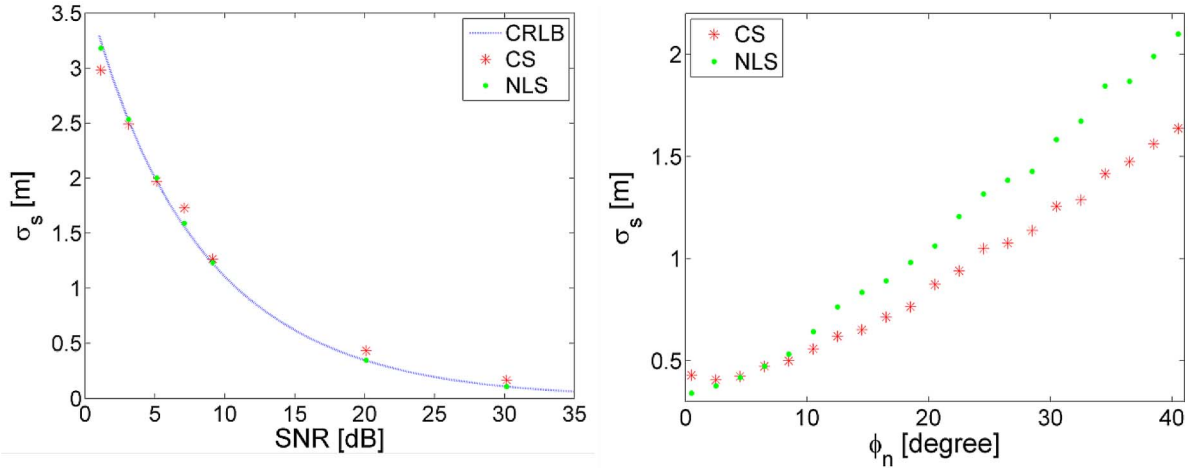

Fig. 7. Single scatterer elevation estimation accuracy of NLS and CS compared to the Cramér–Rao Lower Bound as a function of SNR (left) and as a function of different phase noise levels $[-\phi_n, \phi_n)$ (SNR = 20 dB) (right).

clearly two spectral lines with an accuracy within ± 3 times the CRLB under total SNR = 5 dB [Fig. 5(b)]. With higher SNR, CS is even able to separate closer scatterers. For instance, with SNR = 10 dB, two scatterers with elevations of 0 and 20 m can be well separated [Fig. 5(c)], and with SNR = 20 dB, two scatterers even with elevations of 0 and 5 m can be well separated [Fig. 5(d)].

As multiple scatterers inside one resolution cell most likely occur in high-rise urban areas, the situation in which there are two scatterers inside one resolution cell (one from the building facade and another from the ground) is simulated as an another example to evaluate the performance of the spectral estimation methods. The building is assumed to have an elevation of 80 m, where ground is at zero elevation.

Fig. 8. (Left) Las Vegas Convention Center (Google Earth). (Right) TerraSAR-X intensity map.

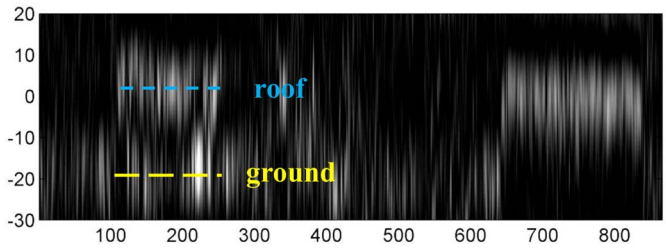

Fig. 9. Estimated reflectivity with SVD-Wiener shown in the azimuth–elevation plane [horizontal: azimuth; vertical: elevation, converted to height (in meters)].

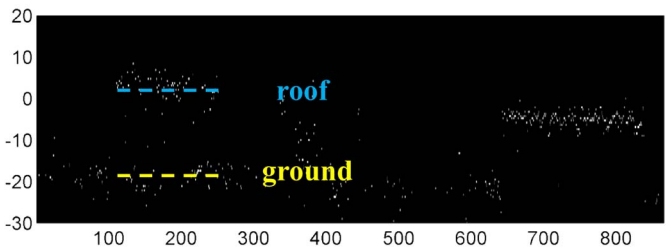

Fig. 10. Same slice as Fig. 9 but estimated by CS.

Fig. 6 shows the estimated elevation values of the two scatterers with maximum detection (MD) [22] (left), nonlinear least squares (NLS) [25] (middle), and CS with different reflectivity ratio (i.e., for the upper plots, the two scatterers have the same reflectivity, while for the lower plots, the (amplitude) reflectivity of the scatterer on the building facade is 0.5 times of the one on the ground). MD simply uses the maxima of the nonparametric SVD-Wiener reconstruction as estimates. The x-axis refers to the true elevation of scatterers on the building facade. The y-axis shows their estimated elevations. The ideal image would be two straight lines (one horizontal and another one diagonal). The green dashed lines in the plots show again ± 3 times the CRLB on elevation estimates for single scatterers.

From Fig. 6, MD shows the resolution limit of classical nonparametric methods. Once the two scatterers are closer than the elevation resolution, only a single maximum in-between the two true positions is detected. Even if the scatterers are farther apart, their sidelobes mutually distort the location of their maxima [e.g., Fig. 6(a)]. The elevation estimates are biased and follow the sidelobe structure of the elevation point response function. NLS is identical to a maximum-likelihood estimator (MLE) and is the theoretically best solution under Gaussian noise and for single scatterers. NLS requires high

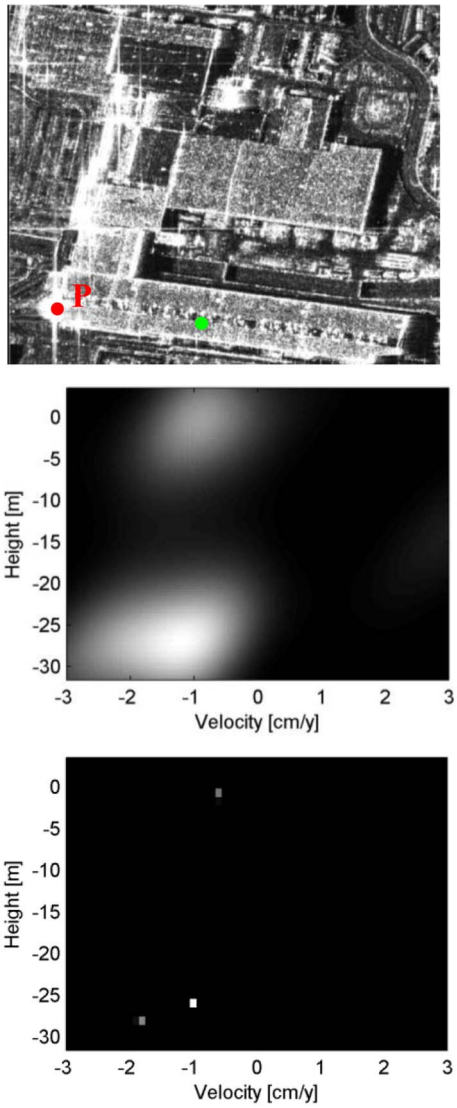

Fig. 11. Four-dimensional reconstruction example. CS versus SVD-Wiener. (Top) TS-X intensity map and analysis point P. (Middle) SVD-Wiener reconstruction results. (Bottom) CS result.

computational effort due to the multidimensional search in elevation. As a parametric method (model-based), we need the *a priori* information about the number of scatterers, i.e., we require model selection and multiple runs of the algorithm for different model orders. This will further increase the computational effort for different hypothesis tests. Compared to MD, CS dramatically improves the elevation resolution under low noise level. For instance, CS is able to reach an elevation separability of about 10 m with SNR $= 10$ dB. In addition, CS shows no sidelobe interference problem, even in the case where one of the two scatterers has a large reflectivity while the other one is much weaker [e.g., Fig. 6(f)]. Compared to NLS, CS is relatively fast and does not require the number of scatterers as *a priori* knowledge. From visual comparison, CS shows similar elevation estimation accuracy as NLS. The estimates of NLS and CS agree well with the CRLB.

In Fig. 7, the left plot shows the elevation estimation accuracy of a single scatterer in the phase-noise-free case using NLS and CS compared to the CRLB under different SNR levels.

NLS as the MLE with Gaussian noise shows an accuracy that is consistent to the CRLB. Moreover, the elevation estimation accuracy of CS for single scatterers is almost identical to that of NLS. The right plot shows the elevation estimation accuracy of a single scatterer using NLS and CS by adding a phase noise uniformly distributed in $[-\phi_n, \phi_n)$ under SNR $= 20$ dB. The estimation accuracy obviously highly depends on the phase noise, and CS is more robust against this type of non-Gaussian noise.

Taking all those aspects into account, CS provides the best of both worlds of nonparametric and parametric spectral estimation methods and is hence proven very attractive for TomoSAR.

C. Real Data

a) CS TomoSAR: The Las Vegas Convention Center is a very interesting test building for 3-D focusing for two reasons. First, it is very big and has a regular shape. Therefore, we are able to check the plausibility of the results. Second, it has a height of about 20 m, the critical distinguishable distance between two scatterers (one from the ground and the other from the building) by using SVD-Wiener for our elevation aperture size. The presence of two scatterers within azimuth–range pixels is expected in layover areas and has been validated by using SVD-Wiener in [22]. Thus, we are able to compare the performance of CS at the layover areas to that of the SVD-Wiener method. The left image in Fig. 8 shows the convention center visualized in Google Earth. The right image is the TerraSAR-X intensity map of the area. We choose a reference pixel according to Adam *et al.* [28], which has most likely only a single scatterer inside. The bright blue line shows the position of the analysis slice, and the area marked by the red block is a layover area. From the Google Earth image, we can see that there is a small triangular-shaped plaza on the ground made of the same material as the building. Thereby, multiple scatterers are expected.

Fig. 9 shows the estimated reflectivity with SVD-Wiener in the azimuth–elevation plane [horizontal: azimuth; vertical: elevation (converted to height)]. Multiple scatterers with marginally distinguishable distance appear (one from the building marked with blue line, and the other from the small structures on the ground marked with yellow line). Even though it demonstrates the stability of SVD-Wiener, the resolution limitation blurs the reflectivity profile for each pixel. In contrast, Fig. 10 shows the same plot as Fig. 9 estimated by the CS approach. Compared to Fig. 9, not only the layover area can be separated but also the elevation positions can be easily located in the reflectivity slice.

b) Differential CS TomoSAR: We have implemented the CS approach to *differential* TomoSAR as well. The top image in Fig. 11 shows again the TerraSAR-X intensity map of the convention center. The pixel P marked by the red dot that locates at the layover area and a reference point (green) on the roof of the building have been taken as an example. Again, two scatterers with slightly different linear deformation in LOS (one from the ground and one from the roof) have been detected in the elevation–velocity plane by SVD-Wiener (middle image). However, the scatterer on the ground appears much brighter and wider. It is very likely to have two scatterers together that are not separable. The bottom image of Fig. 11 shows the result using the CS approach. Two very close scatterers with slightly different heights and velocities (about 2 m in height and 1 cm/y in velocity) have been detected. This signal may be caused by the semicircular structure of the convention center overlaid with the plaza, which can be seen from the Google Earth image.

VI. Conclusion

TomoSAR with very high-resolution spaceborne systems like TerraSAR-X and COSMO-Skymed requires robust inversion algorithms with super-resolution capabilities. Since the elevation profiles to be reconstructed can often be assumed sparse, i.e., they consist only of a small number of pointlike scatterers, the CS framework is applicable. These algorithms use L_1-norm minimization and regularization. Compared to nonparametric and fully parametric L_2-norm methods, they have the following several advantages.

1) CS is more robust than NLS parametric methods with respect to unmodeled phase errors. It does not suffer from self-cancellation artifacts, like CAPON [10].
2) In the single-scatterer case and under Gaussian noise, CS approaches the accuracy of NLS, i.e., the CRLB.
3) CS is computationally more efficient than NLS.
4) For multiple scatterers, CS exhibits a much better resolution than linear nonparametric methods.
5) CS does not need model selection, i.e., it "automatically" chooses the number of scatterers that can be resolved.
6) CS can achieve super resolution in elevation while maintaining the full azimuth–range resolution.

Further work will focus on evaluating the super-resolution power and robustness of this technique, i.e., trying to find its limit.

References

[1] A. Reigber and A. Moreira, "First demonstration of airborne SAR tomography using multibaseline L-band data," *IEEE Trans. Geosci. Remote Sens.*, vol. 38, no. 5, pp. 2142–2152, Sep. 2000.
[2] F. Lombardini, "Differential tomography: A new framework for SAR interferometry," in *Proc. IGARSS*, Toulouse, France, 2003, pp. 1206–1208.
[3] P. Pasquali, C. Prati, F. Rocca, and M. Seymour, "A 3-D SAR experiment with EMSL data," in *Proc. IGARSS*, 1995, pp. 784–786.
[4] J. Homer, D. I. Longstaff, Z. She, and D. Gray, "High resolution 3-D imaging via multi-pass SAR," *Proc. Inst. Elect. Eng.*, vol. 149, no. 1, pt. F, pp. 45–50, Feb. 2002.
[5] Z. She, D. Gray, R. E. Bogner, J. Homer, and I. D. Longstaff, "Three-dimensional spaceborne synthetic aperture radar (SAR) imaging with multipass processing," *Int. J. Remote Sens.*, vol. 23, no. 20, pp. 4357–4382, Oct. 2002.
[6] G. Fornaro, F. Serafino, and F. Lombardini, "Three-dimensional multipass SAR focusing: Experiments with long-term spaceborne data," *IEEE Trans. Geosci. Remote Sens.*, vol. 43, no. 4, pp. 702–714, Apr. 2005.
[7] X. Zhu, N. Adam, and R. Bamler, "First demonstration of space-borne high resolution SAR tomography in urban environment using TerraSAR-X data," in *Proc. CEOS SAR Workshop Calibration Validation*, 2008.
[8] G. Fornaro and F. Serafino, "Imaging of single and double scatterers in urban areas via SAR tomography," *IEEE Trans. Geosci. Remote Sens.*, vol. 44, no. 12, pp. 3497–3505, Dec. 2006.
[9] G. Fornaro, D. Reale, and F. Serafino, "Four-dimensional SAR imaging for height estimation and monitoring of single and double scatterers," *IEEE Trans. Geosci. Remote Sens.*, vol. 47, no. 1, pp. 224–237, Jan. 2009.

[10] F. Lombardini and A. Reigber, "Adaptive spectral estimation for multibaseline SAR tomography with airborne L-band data," in *Proc. IEEE IGARSS*, 2003, vol. 3, pp. 2014–2016.
[11] S. Guillaso and A. Reigber, "Polarimetric SAR tomography (POLTOMSAR)," in *Proc. POLINSAR*, Frascati, Italy, 2005.
[12] F. Gini and F. Lombardini, "Multibaseline cross-track SAR interferometry: A signal processing perspective," *IEEE Aerosp. Electron. Syst. Mag.*, vol. 20, no. 8, pp. 71–93, Aug. 2005.
[13] E. Candès, "Compressive sampling," in *Proc. Int. Congr. Math.*, Madrid, Spain, 2006, vol. 3, pp. 1433–1452.
[14] R. Baraniuk, "Compressive sensing," *IEEE Signal Process. Mag.*, vol. 24, no. 4, pp. 118–121, Jul. 2007.
[15] D. Donoho, "Compressed sensing," *IEEE Trans. Inf. Theory*, vol. 52, no. 4, pp. 1289–1306, Apr. 2006.
[16] E. Candès, J. Romberg, and T. Tao, "Robust uncertainty principles: Exact signal reconstruction from highly incomplete frequency information," *IEEE Trans. Inf. Theory*, vol. 52, no. 2, pp. 489–509, Feb. 2006.
[17] L. Zhang, M. Xing, C. Qiu, J. Li, and Z. Bao, "Achieving higher resolution ISAR imaging with limited pulses via compressed sampling," *IEEE Geosci. Remote Sens. Lett.*, vol. 6, no. 3, pp. 567–571, Jul. 2009.
[18] A. Budillon, A. Evangelista, and G. Schirinzi, "SAR tomography from sparse samples," in *Proc. IEEE IGARSS*, Cape Town, Africa, 2009, pp. IV-865–IV-868.
[19] X. Zhu and R. Bamler, "Very high resolution spaceborne SAR tomography in urban environment," *IEEE Trans. Geosci. Remote Sens.*, to be published.
[20] G. Fornaro, F. Serafino, and F. Soldovieri, "Three-dimensional focusing with multipass SAR data," *IEEE Trans. Geosci. Remote Sens.*, vol. 41, no. 3, pp. 507–517, Mar. 2003.
[21] L. Gan, C. Ling, T. T. Do, and T. D. Tran, *Analysis of the Statistical Restricted Isometry Property for Deterministic Sensing Matrices Using Stein's Method*, 2009, (Preprint).
[22] S. Chen, D. Donoho, and M. Saunders, "Atomic decomposition by basis pursuit," *SIAM J. Sci. Comput.*, vol. 20, no. 1, pp. 33–61, 1998.
[23] D. K. Hammond, L. Jacques, M. J. Fadili, G. Puy, and P. Vandergheynst, The Basis Pursuit DeQuantizer (BPDQ) Toolbox, Signal Processing Laboratory (LTS2), EPFL, Lausanne, Switzerland, Jul. 2009. [Online]. Available: http://wiki.epfl.ch/bpdq
[24] M. Eineder, N. Adam, R. Bamler, N. Yague-Martinez, and H. Breit, "Spaceborne spotlight SAR interferometry with TerraSAR-X," *IEEE Trans. Geosci. Remote Sens.*, vol. 47, no. 5, pp. 1524–1535, May 2009.
[25] S. D'Amico, C. Arbinger, M. Kirschner, and S. Campagnola, "Generation of an optimum target trajectory for the TerraSAR-X repeat observation satellite," in *Proc. 18th Int. Symp. Space Flight Dyn.*, Munich, Germany, 2004.
[26] R. Bamler, M. Eineder, N. Adam, X. Zhu, and S. Gernhardt, "Interferometric potential of high resolution spaceborne SAR," *Photogramm. Fernerkundung Geoinf.*, vol. 2009, no. 5, pp. 407–419, Nov. 2009.
[27] X. Zhu, N. Adam, R. Brcic, and R. Bamler, "Space-borne high resolution SAR tomography: Experiments in urban environment using TerraSAR-X data," in *Proc. JURSE*, 2009.
[28] N. Adam, R. Bamler, M. Eineder, and B. Kampes, "Parametric estimation and model selection based on amplitude-only data in PS-interferometry," in *Proc. FRINGE-Workshop*, Frascati, Italy, 2005.

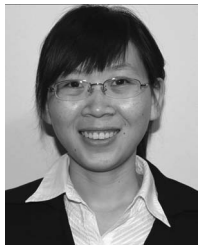

Xiao Xiang Zhu (S'10) was born in Changsha, China, on December 12, 1984. She received the B.S. degree in space engineering from the National University of Defense Technology, Changsha, in 2006 and the M.Sc. degree in earth oriented space science and technology (ESPACE) from the Technische Universität München (TUM), München, Germany, in 2008. She is curently working toward the Ph.D. degree in differential synthetic aperture radar (SAR) tomography using TerraSAR-X data at the Remote Sensing Technology, TUM.

Since May 2008, she has been a Full-Time Scientific Collaborator with Remote Sensing Technology, TUM. Her work is part of the project team "Dynamic Earth," which was established in the International Graduate School of Science and Engineering, TUM, as a result of the German Excellence Initiative in 2007. In October/November 2009, she was a Guest Scientist with the Institute for Electromagnetic Sensing of the Environment (IREA), Italian National Research Council (CNR), Naples, Italy. Her main research interests are in the signal processing field with applications to spaceborne SAR data, in particular SAR tomography, and differential SAR tomography.

Richard Bamler (M'95–SM'00–F'05) received the Diploma degree in electrical engineering, the Doctor of Engineering degree, and the "Habilitation" degree in signal and systems theory from the Technische Universität München (TUM), München, Germany, in 1980, 1986, and 1988, respectively.

During 1981 and 1989, he was with TUM, working on optical signal processing, holography, wave propagation, and tomography. In 1989, he joined the German Aerospace Center (DLR), Oberpfaffenhofen, Germany, where he is currently the Director of the Remote Sensing Technology Institute (IMF). Since then, he and his team have been working on synthetic aperture radar (SAR) signal processing algorithms (ERS, SIR-C/X-SAR, Radarsat, SRTM, ASAR, TerraSAR-X, and TanDEM-X), SAR calibration and product validation, SAR interferometry, phase unwrapping, estimation theory and model-based inversion methods for atmospheric sounding (GOME, SCIAMACHY, MIPAS, and GOME-2), and oceanography. In early 1994, he was a Visiting Scientist with the Jet Propulsion Laboratory in preparation of the SIC-C/X-SAR missions, and in 1996, he was a Guest Professor with the University of Innsbruck, Innsbruck, Austria. Since 2003, he has been a Full Professor in remote sensing technology with TUM. His current research interests are in algorithms for optimum information extraction from remote sensing data with emphasis on SAR, SAR interferometry, persistent scatterer interferometry, SAR tomography, and ground moving target indication for security-related applications. He and his team have developed and are currently developing the operational processor systems for the German missions TerraSAR-X, TanDEM-X, and EnMAP. He is the author of more than 160 scientific publications, among them about 40 journal papers, a book on multidimensional linear systems theory, and several patents on SAR signal processing.